Supporting Information

Photothermal self-adjuvant porous microneedles for self-healing encapsulation and sustained release of antigens to improve adaptive immunity

Xin Wang [a,b], Zhiming Li [b], Jiahui Fu [a,b], Xueyu Wen [b], Zhenni Chen [b], Shaohua Li [b], Tianqi Liu [b,*], Fei Jia [b,*], Hao Chang [b,*]

[a] College of Materials Science and Engineering, Zhejiang University of Technology, Hangzhou, Zhejiang, 310014, China.

[b] Hangzhou Institute of Medicine, Chinese Academy of Sciences, Hangzhou, Zhejiang 310022, China

*Corresponding author

Email: liutianqi@him.cas.cn (T.Q. Liu), jiafei@him.cas.cn (F. Jia), changhao@him.cas.cn (H. Chang).

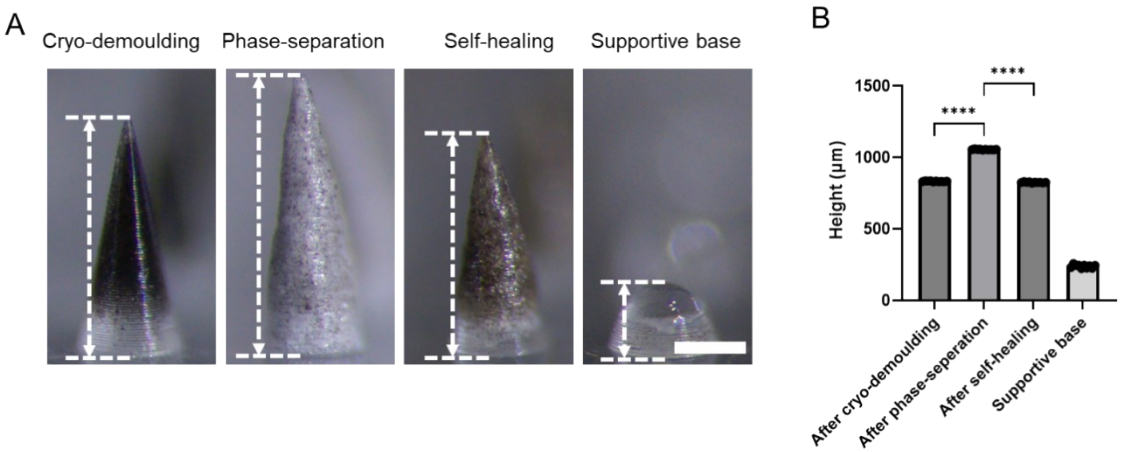

Figure S1. Morphological development of H-PSAPMNs during fabrication. (A) Representative microscopy of MNs after cryo-demolding, phase-separation, self-healing, and separation. Scale bar: 250 µm. (B) Statistical analysis of the heights of cryogenically demolded MNs, PSAPMNs, H-PSAPMNs, and the supportive cap. Data are presented as mean ± s.d. (n = 10). $p < 0.05$, $^{**}p < 0.01$, $^{***}p < 0.001$, $^{****}p < 0.0001$, ns = no significant difference.

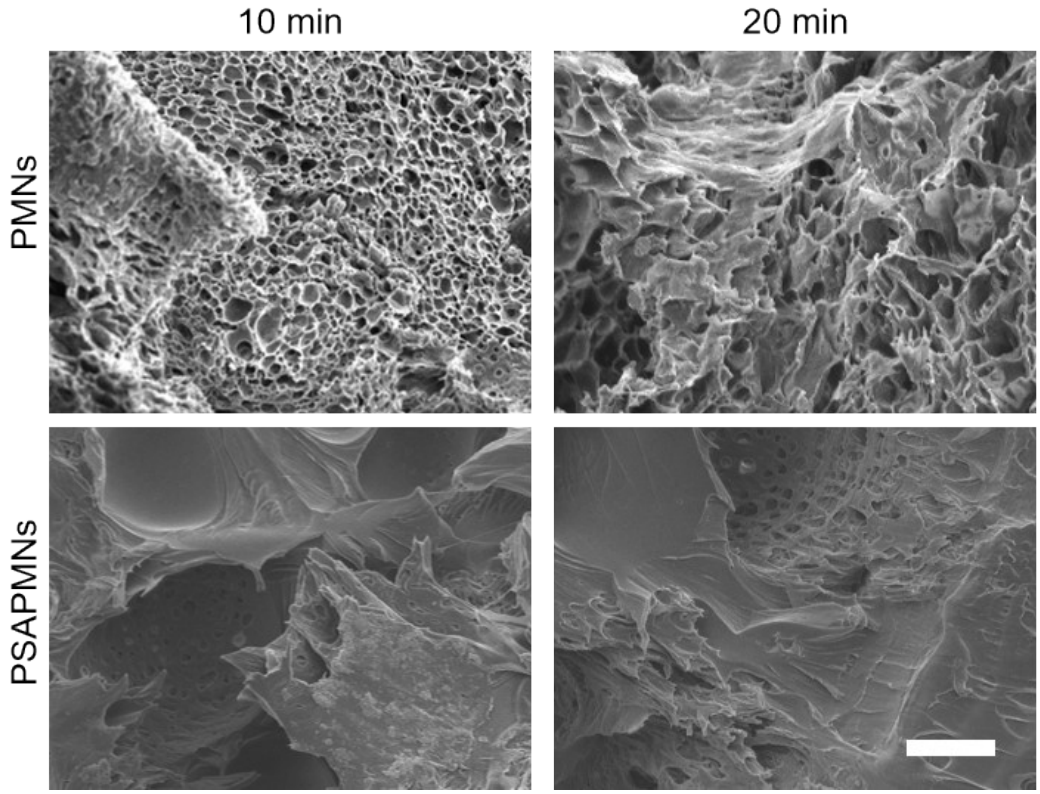

Figure S2. Self-healing behavior of PSAPMNs. High-magnification cross-sectional SEM images of PMNs and PSAPMNs subjected to NIR irradiation (0.6 W/cm^2) for varying durations. Scale bars: 20 μm.

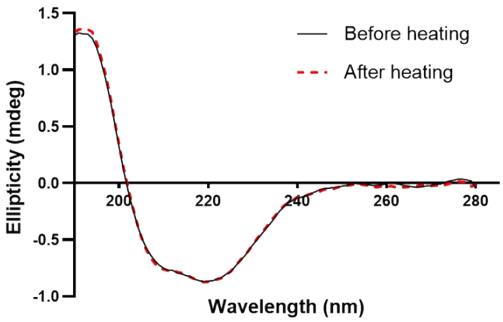

Figure S3. Structural integrity of OVA. Circular dichroism (CD) spectra of native OVA (black line) and OVA recovered from H-PSAPMNs after heating treatment at 45 °C for 90 minutes (red dashed line).

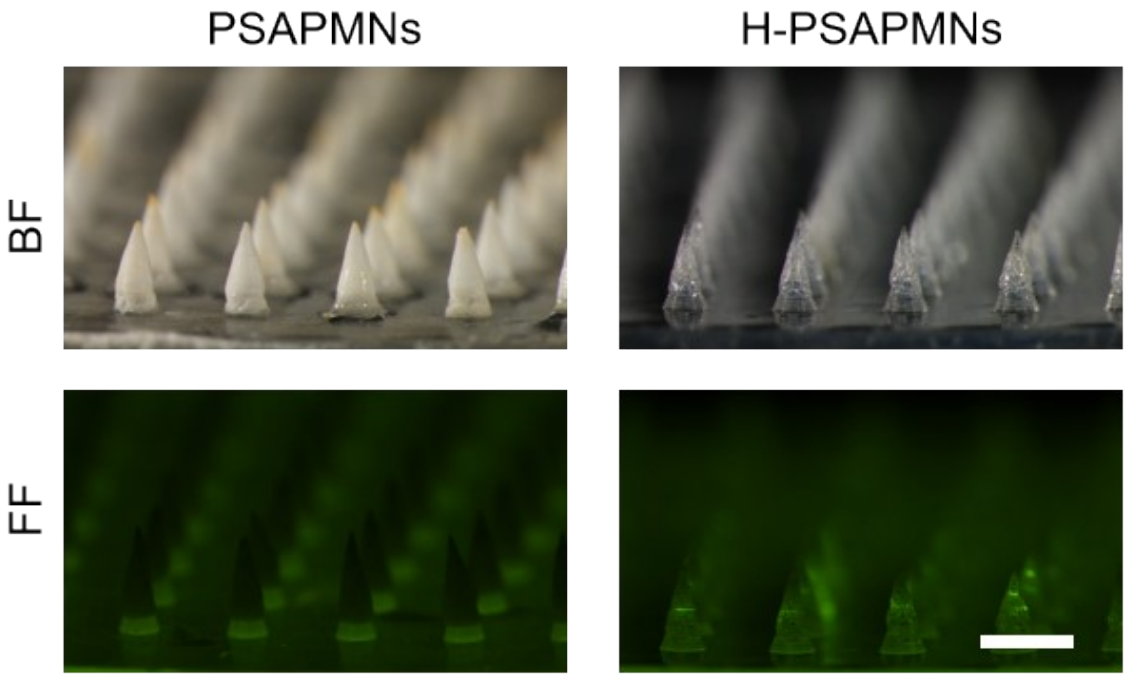

Figure S4. Antigen sealing performance. Representative bright-field and fluorescence microscopy images of PSAPMNs and H-PSAPMNs (both loaded with FITC-OVA) after immersion in a water bath. Scale bar: 1000 μm.

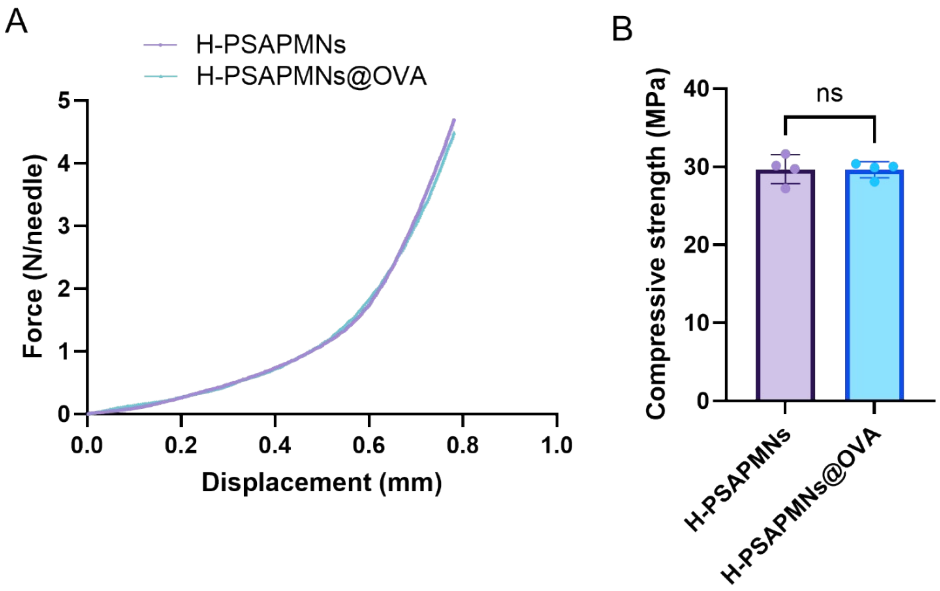

Figure S5. (A) Force-displacement curve for H-PSAPMNs and H-PSAPMNs loaded with OVA. (B) Compressive strength of H-PSAPMNs and H-PSAPMNs loaded with OVA. Data are presented as mean ± s.d. (n = 4). ns = no significant difference.

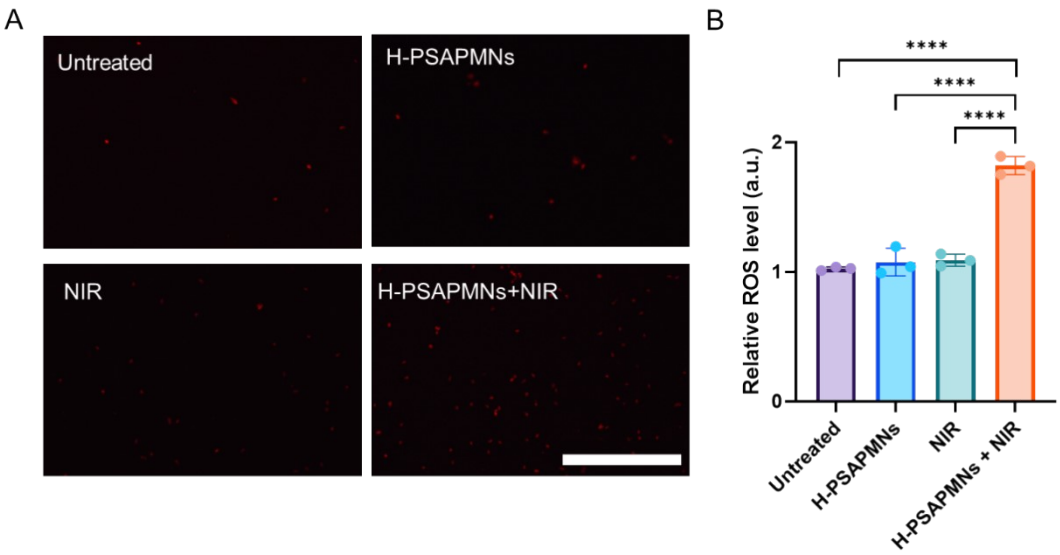

Figure S6. Reactive oxygen species (ROS) generation in mouse skin following various treatments. (A) Representative fluorescence microscopy images showing ROS levels in skin tissues from four groups: untreated control, H-PSAPMNs, NIR irradiation (10 min), and H-PSAPMNs combined with NIR irradiation (10 min). Scale bar: 500 μm. (B) Quantitative analysis of relative ROS levels among the treatment groups. Data are presented as mean ± s.d. (n = 4). ****$P < 0.0001$.

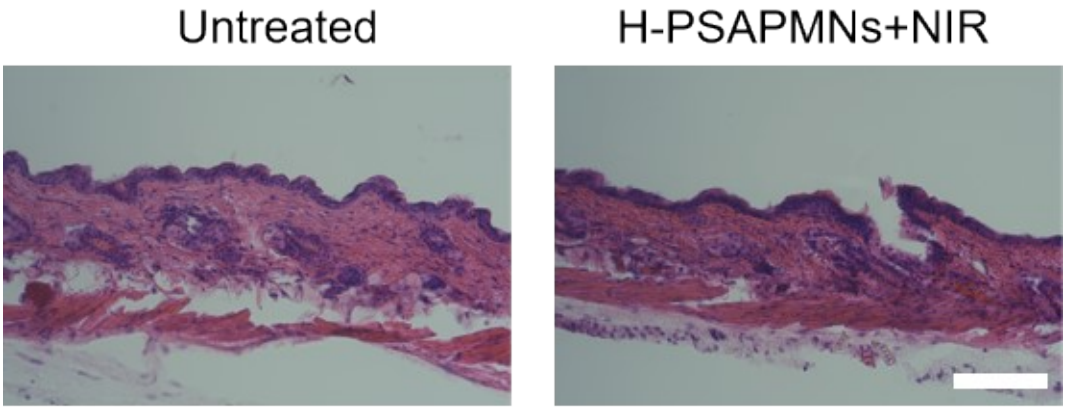

Figure S7. Histological evaluation of skin safety after photothermal treatment. Representative H&E-stained sections of skin tissues collected 24 hours post-treatment from the untreated group and the H-PSAPMNs + NIR group. Scale bar: 200 μm.

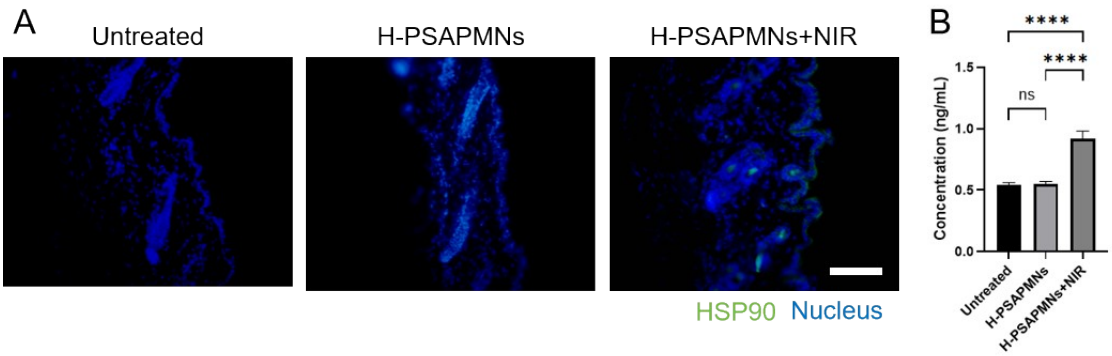

Figure S8. Evaluation of HSP90 expression in skin tissues. (A) Representative immunofluorescence images of skin sections stained for HSP90 (green) and nuclei (blue) from the untreated, H-PSAPMNs, and H-PSAPMNs+NIR groups. Scale bar = 200 μm. (B) Quantitative analysis of HSP90 levels in skin tissue homogenates measured by ELISA. Data are presented as mean ± s.d. (n = 3). ****$p < 0.0001$, ns = no significant difference.

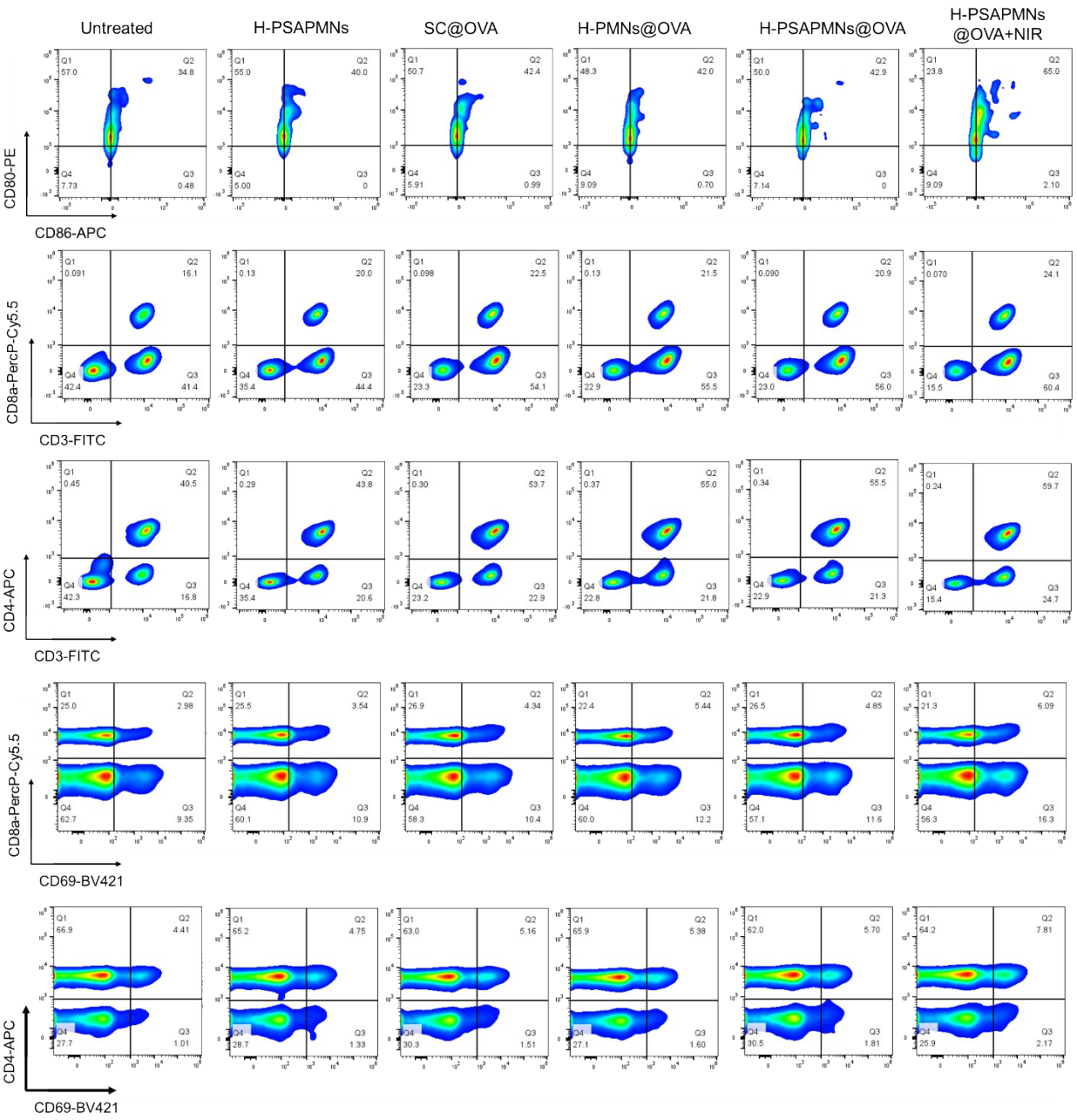

Figure S9. Representative flow cytometry plots illustrating the percentages of $CD80^+CD86^+$ DCs, $CD8^+CD3^+$ T cells, $CD4^+CD3^+$ T cells, $CD8^+CD69^+$ T cells, and $CD4^+CD69^+$ T cells in draining lymph nodes (dLNs) isolated from mice across different vaccination groups.

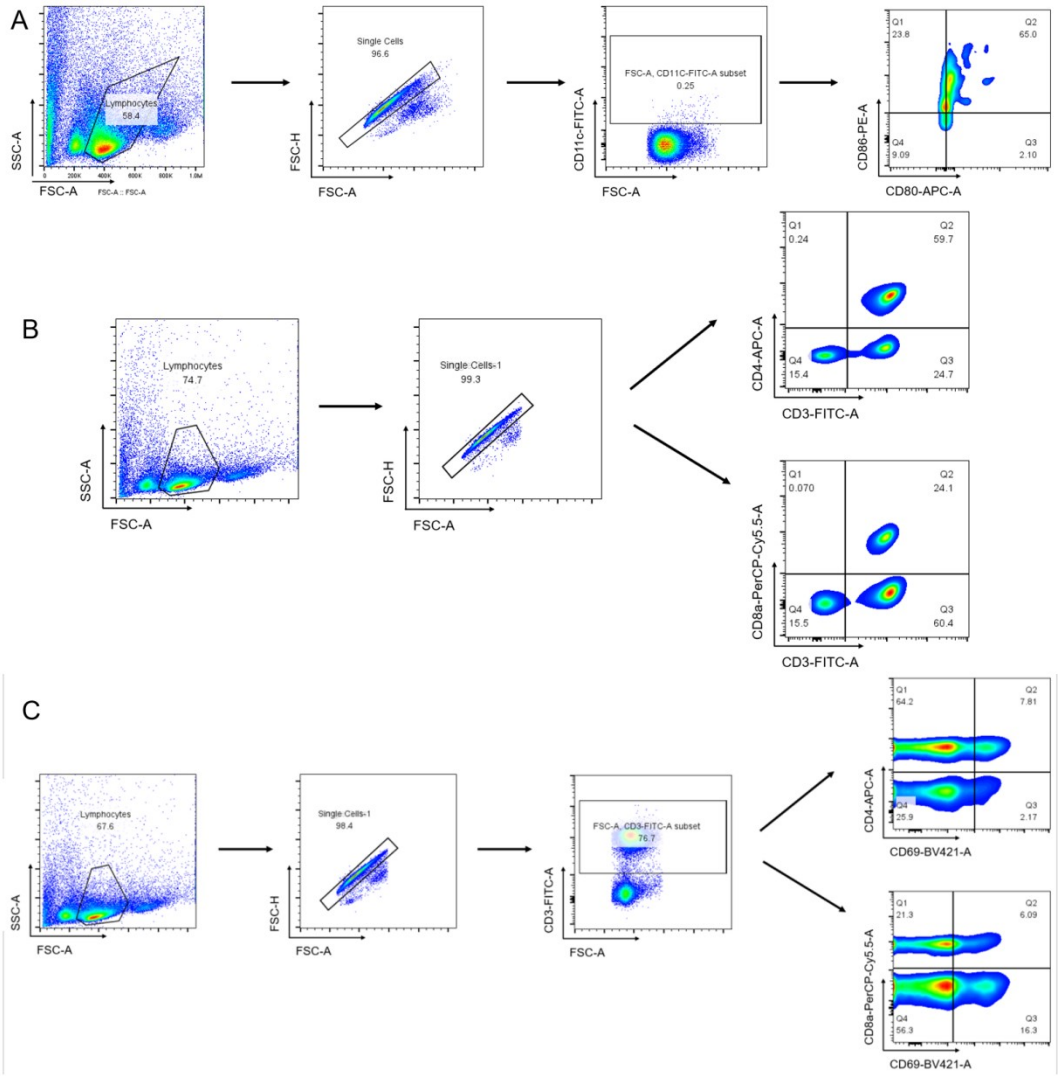

Figure S10. Flow cytometry gating strategy for immune cells in draining lymph nodes. Total lymphocytes were first gated based on the FSC-A and SSC-A, and single cells were gated based on FSC-A and FSC-H. Data were analyzed using FlowJo software, and expressed as a percent of (A) $CD80^+CD86^+$ DCs. (B) $CD3^+CD4^+$ T cells and $CD3^+CD8^+$ T cells. (C) $CD69^+CD4^+$ T cells and $CD69^+CD8^+$ T cells.

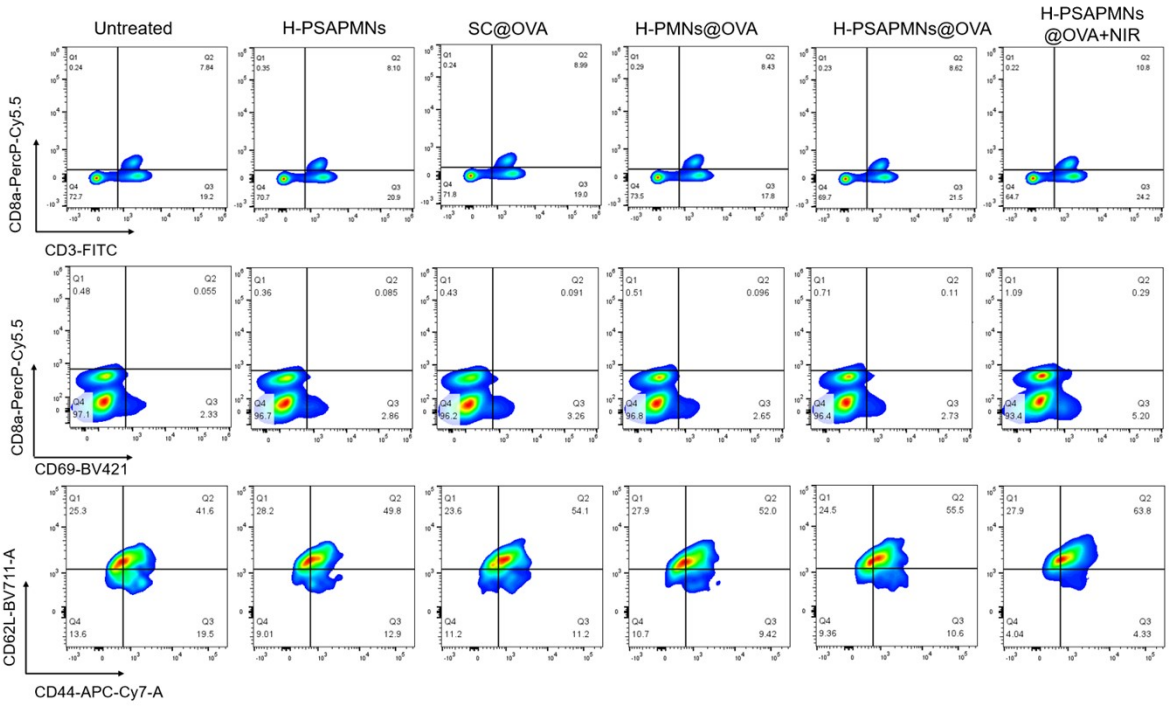

Figure S11. Representative flow cytometry plots illustrating the percentages of $CD3^{+}CD8^{+}$ T cells, $CD8^{+}CD69^{+}$ T cells, and $CD8^{+}$ memory T cells in spleen isolated from mice across different vaccination groups.

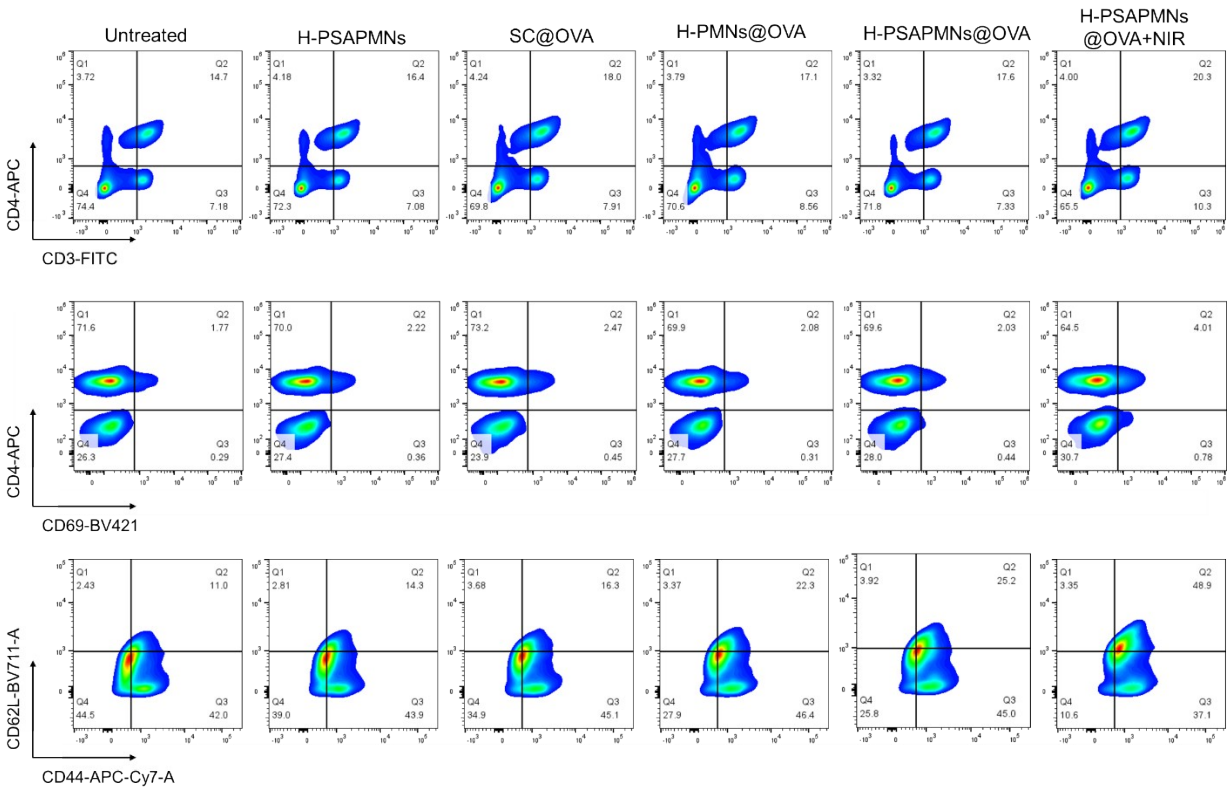

Figure S12. Representative flow cytometry plots illustrating the percentages of $CD3^+CD4^+$ T cells, $CD4^+CD69^+$ T cells, and $CD4^+$ memory T cells in spleen isolated from mice across different vaccination groups.

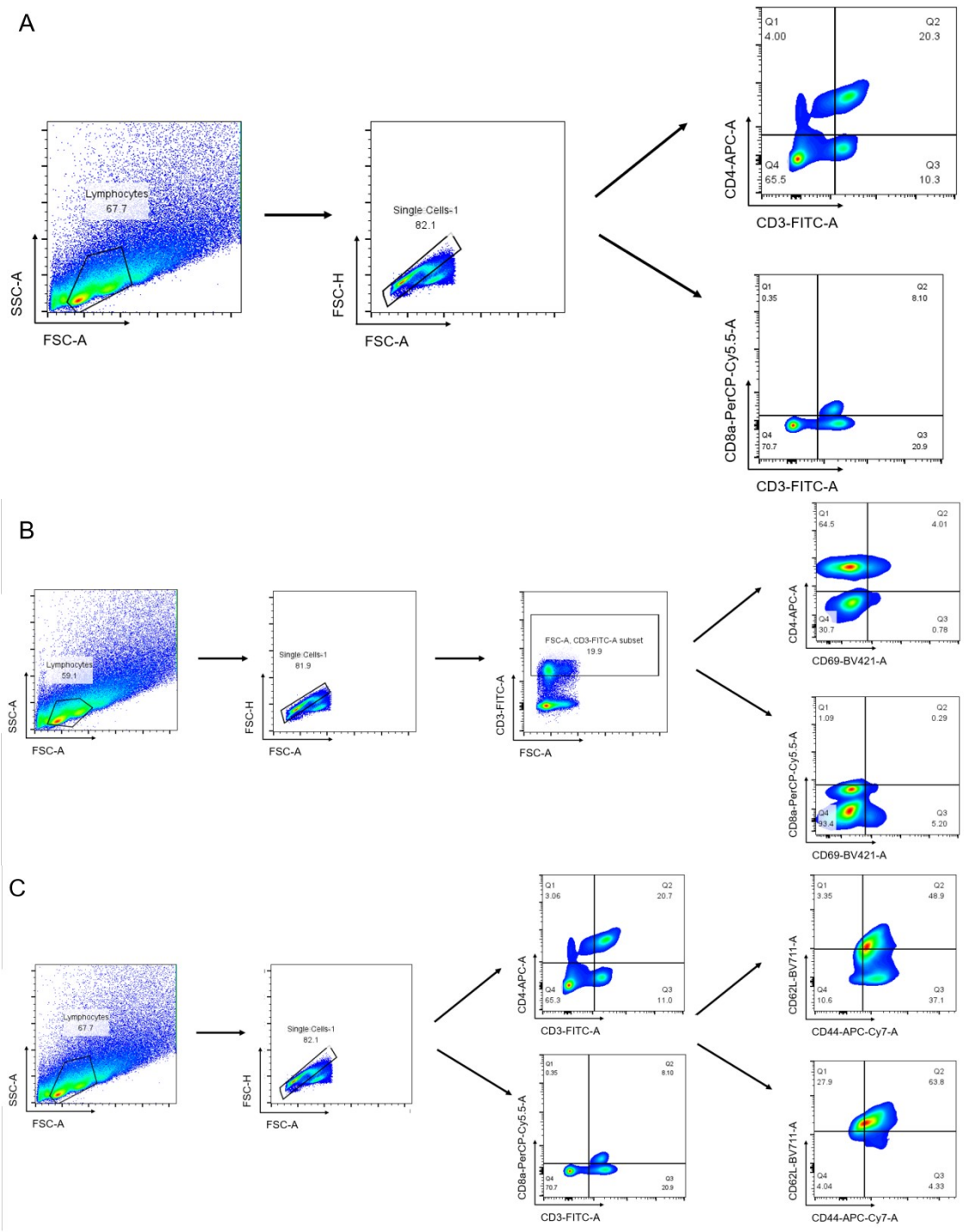

Figure S13. Flow cytometry gating strategy for immune cells in the spleen. Total lymphocytes were first gated based on FSC-A and SSC-A, and single cells were gated based on FSC-A and FSC-H. Data were analyzed using FlowJo software and are expressed as a percent of: (A) $CD3^+CD4^+$ and $CD3^+CD8^+$ T cells. (B) $CD69^+CD4^+$ and $CD69^+CD8^+$ T cells. (C) $CD44^+$ and $CD62L^+$ memory T cells.